ADVANCED MATERIALS
www.advmat.de

Multiscale Heterogeneous Polymer Composites for High Stiffness 4D Printed Electrically Controllable Multifunctional Structures

*Javier M. Morales Ferrer, Ramón E. Sánchez Cruz, Sophie Caplan, Wim M. Van Rees, and J. William Boley**

4D printing is an emerging field where 3D printing techniques are used to pattern stimuli-responsive materials to create morphing structures, with time serving as the fourth dimension. However, current materials utilized for 4D printing are typically soft, exhibiting an elastic modulus (E) range of 10^{-4} to 10 MPa during shape change. This restricts the scalability, actuation stress, and load-bearing capabilities of the resulting structures. To overcome these limitations, multiscale heterogeneous polymer composites are introduced as a novel category of stiff, thermally responsive 4D printed materials. These inks exhibit an E that is four orders of magnitude greater than that of existing 4D printed materials and offer tunable electrical conductivities for simultaneous Joule heating actuation and self-sensing capabilities. Utilizing electrically controllable bilayers as building blocks, a flat geometry is designed and printed that morphs into a 3D self-standing lifting robot, setting new records for weight-normalized load lifted and actuation stress when compared to other 3D printed actuators. Furthermore, the ink palette is employed to create and print planar lattice structures that transform into various self-supporting complex 3D shapes. These contributions are integrated into a 4D printed electrically controlled multigait crawling robotic lattice structure that can carry 144 times its own weight.

1. Introduction

Responsive materials have emerged as a focal point for researchers over the past decade, driven by their versatile applications within smart material systems. These systems are defined as smart due to their ability to change shape in response to stimuli such as change in temperature, electric, or magnetic field.[1] Notably, they exhibit potential across a spectrum of applications such as energy-harvesting systems.[2] smart actuators.[3] smart textiles.[4] and even in the development of robotic exoskeletons.[1,2] Among the commonly employed responsive systems are piezoelectrics, magnetostrictive materials, pneumatic systems, dielectric elastomers, and shape memory alloys (SMAs).[1] SMAs, in particular, stand out as preferred materials for responsive applications, primarily due to their ability to achieve localized actuation through Joule heating and their inherently high actuation stress.[1,5] Nevertheless, it is crucial to underscore that one of the paramount challenges associated with SMAs is limited complexity.[5] Recent strides in SMA technology have harnessed 3D printing techniques to confront this challenge.[6,7] Despite these advancements, 3D printable SMAs still have practical limitations due to the insufficient shape-memory effect.[5–7] Moreover, whether employing conventional manufacturing methods or adopting 3D printable approaches, SMAs consistently exhibit low repeatability, low reversibility, and necessitate additional pre-programming steps before or after they are manufactured.[5,8] This process involves configuring the SMAs into the target shape, heating it above the martensite phase (≈500 °C), and subsequently cooling it down to the austenite phase (≈25 °C).[5–7] In light of these challenges, there is an increasing demand for materials that are not only responsive, but also possess enhanced reversibility that seamlessly align with fabrication approaches to enable complex shape change. This growing need has ignited extensive research into a spectrum of materials and innovative fabrication approaches, demonstrating considerable potential for effectively addressing these limitations.

A particularly promising avenue lies in the innovative realm of 4D printing, a rapidly emerging field where 3D printed stimuli-responsive materials produce morphing and multifunctional structures, incorporating time as the fourth dimension.[9–12] This

J. M. M. Ferrer, R. E. S. Cruz, S. Caplan, J. W. Boley
Mechanical Engineering Department
Boston University
Boston, MA 02215, USA
E-mail: jwboley@bu.edu
W. M. Van Rees
Department of Mechanical Engineering
Massachusetts Institute of Technology
Cambridge, MA 02139, USA
J. W. Boley
Division of Materials Science and Engineering
Boston University
Boston, MA 02215, USA
The ORCID identification number(s) for the author(s) of this article can be found under https://doi.org/10.1002/adma.202405505

DOI: 10.1002/adma.202405505

approach enables the 3D printing of pre-programed responsive sheets, which transition into complex surfaces upon exposure to external stimuli, resulting in a substantial reduction in material consumption and printing time (70-90%).[9–11] Unlike SMAs, the programming of these responsive structures is achieved through the strategic arrangement of multiple materials in three-dimensional (3D) space, employing the printing process to invoke reversible shape change (e.g., aligning magnetic,[13] anisotropic fillers,[10,12,14,15] and polymer chains.[16]). These morphing structured systems have potential for myriad applications, from deployable systems[12,17,18] and dynamic optics[19,20] to soft robotics[21,22] and frequency-shifting antennae.[12,23] The current materials palette for 4D printing is comprised solely of soft polymer composites (elastic modulus range 10^{-4} – 10 MPa), such as hydrogels.[9,10,24] shape memory polymers (SMPs).[16,25–27] liquid crystal elastomers (LCEs).[15,22,28–30] and poly(dimethylsiloxane) (PDMS).[12,13,31] Hydrogels can be tailored for printable applications, where the printed structures demonstrate reversible swelling upon immersion in water.[9,10,24] However, these materials are restricted to moist environments, and their elastic modulus (E) (0.02 – 1.3 MPa) is the lowest of any 4D printing materials. On the other hand, shape memory polymers (SMPs) are thermoplastic materials that can be programed to change shape in response to temperature by heating the material above its glass transition temperature (T_g), stretching it, and cooling it below T_g.[16,25–27] SMPs demonstrate a higher E in their crystalline state, extending from 10 to 3000 MPa. However, it is important to note that the mechanism of this glass transition-based response is irreversible, necessitating pre-strain for the desired transformation. Moreover, during the glass transition, there is a significant drop in E (ranging from 0.1 to 10 MPa).[25–27] which places them within a similar range as hydrogels. LCEs have been used in 4D printing as well.[15,22,28–30] These materials exhibit a higher E compared to hydrogels, and their functionality is not confined to moist environments. Importantly, LCEs possess the capacity for reversible actuation, attributed to the reversible phase change of aligned mesogens.[15] However, their E is on par with SMPs in their rubbery state (ranging from 1.2 to 12 MPa), thereby sharing similar limitations regarding low E.[15,22,28–30] Moreover, PDMS composites have recently joined the array of 4D printing materials. Previous studies have demonstrated the versatility of these materials, revealing their capability to be blended with various fillers to create responsive inks suitable for 3D printable technologies. These inks can be tailored to respond to external stimuli such as magnetic fields,[13] solvent swelling,[12,32] or temperature variations.[12] It is noteworthy that akin to previous materials, these composites also share a characteristic low modulus (ranging from 0.01 to 1.2 MPa), presenting analogous limitations to hydrogels, SMPs, and LCEs. A comparison of E for these materials is detailed in Table S1 (Supporting Information). It is evident that all these materials share a common limitation of low E while undergoing actuation. This limitation inherently restricts actuation stress, load-bearing capabilities, and the structural integrity of printed objects to support their own weight when increasing the overall dimensions of the printed parts (see SI Methods: Spherical cap scaling analysis). Therefore, an existing challenge for 4D printing is to develop materials that can maintain the large, reversible, and predictable morphing actuation mechanism for complex shape transformation, while significantly advancing the E for high performance applications.[24]

In addition to these challenges related to low E, many existing approaches rely on passive structures that necessitate the control of global conditions of the surrounding environment (e.g., water or solvent baths, ovens, or external magnets) to provide the stimulus for actuation.[12,13,15,26,29,33] thus limiting their range of applications. Recently, researchers have tackled this challenge by integrating electrically conductive materials to create responsive and electrically controllable composites, which enables the introduction of local and addressable stimuli through electrical signals.[22,34] However, it is important to note that the integration of additional materials solely for the purpose of inducing actuation (e.g., Joule heating) can hinder the actuation responsiveness.[15,22,29,35,36] (see SI Methods: Performance of prior work electrically controllable responsive composite). This is because these additional materials do not contribute to the actuation mechanism; instead, they inadvertently introduce extra weight or mechanical constraints that work against the intended actuation. Most recently, successful attempts have been made to integrate conductive materials into responsive composites (e.g., piezoelectrics) while preserving both responsiveness and load-bearing capacity, but require high-temperature sintering of piezoelectric materials, exceeding 1000 °C.[34]

To overcome the presented limitations on the E and localized and addressable actuation, we introduce multiscale heterogeneous polymer composites as a novel category of stiff, electrically controllable 4D printed materials (**Figure 1a**). We call these composites heterogeneous because they contain a plurality of ingredients, including a polymer matrix with an adjustable crosslink density, and a variety isotropic and anisotropic nanoscale and microscale fillers to achieve targeted resulting properties (Figure 1b). Leveraging this platform, we generate a set of 37 inks covering a broad range of negative and positive linear coefficients of thermal expansion (−19.1 ± 0.3 – 128.8 ± 1.2 ppm $°C^{-1}$) (Figure 1c). This set of inks exhibits an E range that is four orders of magnitude greater than that of existing 4D printed materials (0.34 ± 0.1 – 38.6 ± 1.4 GPa) (Figure 1c) and offers tunable electrical conductivities (0.7 ± 0.1 – 3.5×10^3 ± 9.9 S m^{-1}) (Figure 1d) for simultaneous Joule heating actuation and self-sensing capabilities, all while maintaining comparable thermal responsiveness to the state of the art.[12] (Figure 1c). Utilizing electrically controllable bilayers as building blocks, we design and print a flat geometry that changes shape into a 3D self-standing lifting robot, setting new records for lifting capabilities (≈888 times its own weight) and actuation stress (≈6 MPa) when compared to other 3D printed actuators. We integrate this lifting robot with a closed-loop control system, achieving autoregulated actuation exhibiting a 4.8% overshoot and 0.8% undershoot, while effectively rejecting disturbances of up to 170 times the robot's weight, thereby establishing a new record in performance. Furthermore, we employ our ink palette to create, and 3D print planar lattice structures that transform into various self-supporting complex 3D surfaces. Ultimately, we employ our new ink palette to achieve a 4D printed electrically controlled multigait crawling robotic lattice structure equipped with electroadhesive feet, highlighting its capacity to transport loads up to 144 times its own weight.

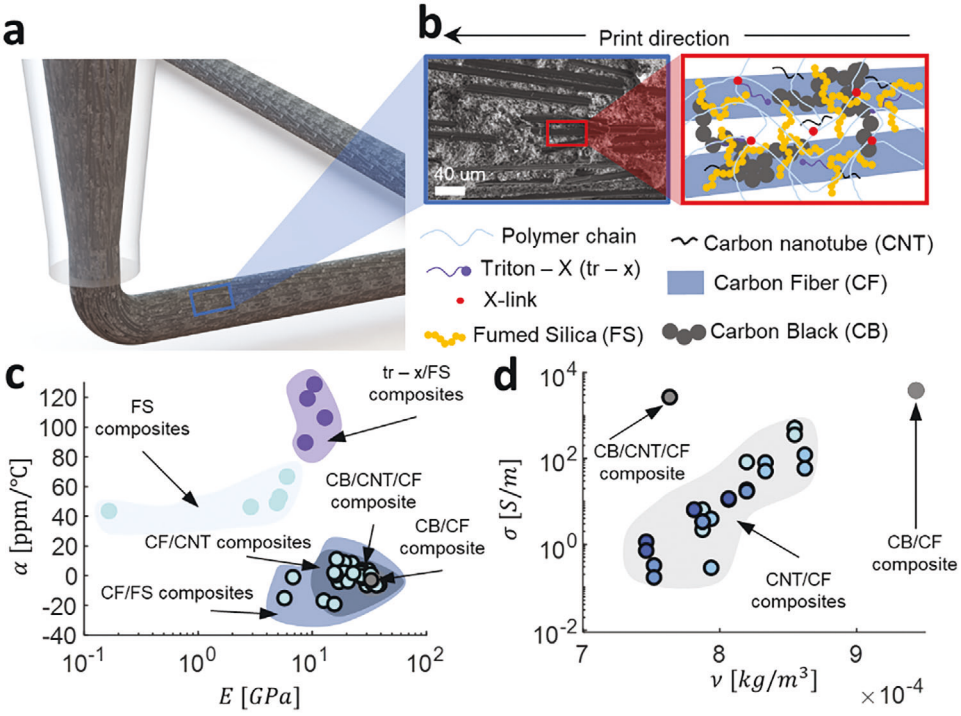

Figure 1. Printable heterogeneous epoxy composite inks with tailored coefficient of thermal expansion (α) elastic modulus (E), electrical conductivity (σ), and specific volume (ν). a) Schematic of 4D printed filament. b) SEM of 3D printed CF composite ink showing alignment of CFs (top-left). Representative notional schematic of all ingredients employed in the development of these heterogeneous polymer composites. (top-right). Legend of ingredients (bottom) c) Range of achievable α and E for these composites. d) Range of achievable σ and ν for these composites. Data extracted from material characterization developed in this work (See Table S3, Supporting Information).

2. Results and Discussion

2.1. Summary of Materials Approach

Our ink design starts with a cycloaliphatic epoxy resin, a thermoset that exhibits a large range of operating temperature (−62 C – 288 °C), high elastic modulus (≈5 GPa), positive α (≈40 ppm °C^{-1}), and low electrical conductivity (<10^{-12} S m^{-1}).[37] This epoxy system was chosen since it can be polymerized at high temperatures (up to 250 °C), allowing us to use ambient cooling to achieve 3D morphing from flat printed structures. **Figure 2**a lists all the tunable material parameters used to synthesize these inks. To develop inks with tunable stiffness and thermal expansion suitable for direct ink writing (DIW) (i.e., a shear-yielding stress, shear-thinning response, and plateau storage modulus) (Figure S1, Supporting Information), we start by adding different volume fractions (5 – 15% v/v) of carbon fibers (CFs), that preferentially align along the print direction due to the shear induced by the nozzle while printing (Figure 1b; Figure S2, Supporting Information).[14] Additionally, carbon nanotubes (CNTs) were added to further improve E, α, rheological, and electrical properties. To further tune the rheological and electrical properties of the composite inks, we included carbon black (CB) ranging from 4% – 8% v/v. Fumed silica (FS) was added to the formulations that do not include CB or CNTs (9 – 12% v/v), solely as a means of tuning the rheological properties to be compatible with DIW (Figure S1, Supporting Information). Moreover, as an additional means of tuning E and α, we vary the cross-linker to base to weight ratio within the epoxy matrix. Finally, we explored different concentrations of non-ionic surfactant (Triton-x (tr-x)), as means of increasing the α and E. All formulations for this study can be found in Table S2 (Supporting Information).

2.2. Resulting Effective E, α, and σ

Figure 2b–d reports the results on the tunable E, α, and σ along the print direction. First, we observe a minimal effect on E, α, and σ due to the inclusions of FS on the different cross-linker to base weight ratio formulations that do not contain CB or CNTs. However, these FS inclusions impart rheological properties suitable for DIW (Figure S1, Supporting Information). Furthermore, we observe an increase in E and α as we added concentrations of tr-x (Figure 2b,c), which has been shown to act as a plasticizer into an epoxy matrix.[38] Recent work has shown that in concentrations lower than 30% v/v, antiplasticization occurs, resulting in a slight improvement in E of the polymer.[39] which is attributed to a suppression of the glassy state mobility. The presence of surfactant in the polymer also slightly reduces T_g, leading to a generation of excess free volume, which in turn increases α.[40] There is a significant improvement on the composite elastic modulus as we increase the content of CFs (Figure 2b) due to the highly aligned networks of CFs along the print direction (Figures S2 and S3, Supporting Information).[14,41,42] The Halpin-Tsai micromechanical model (SI Methods) was used to predict the improvement in E due to the contributions of these CFs fillers (dotted

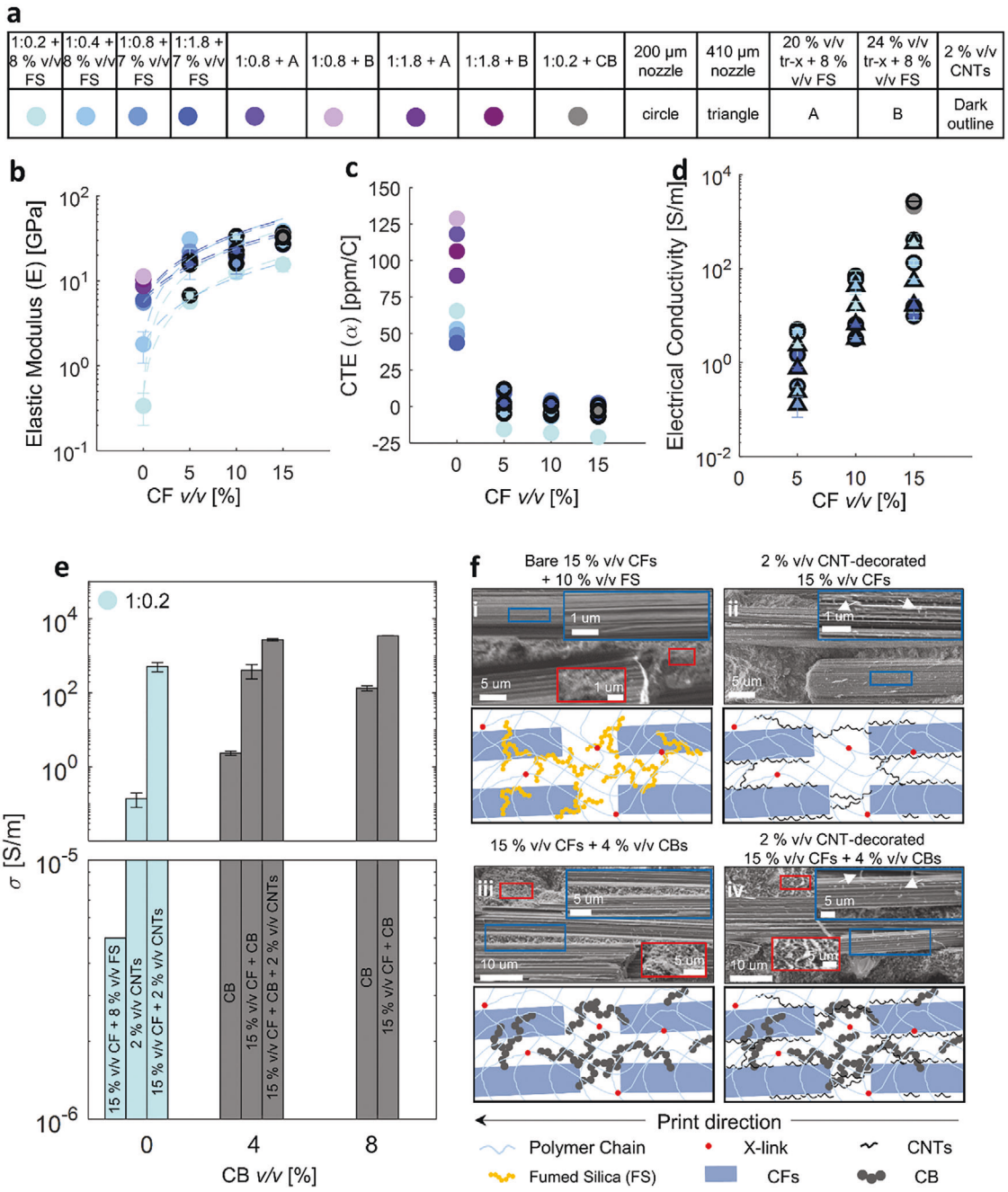

Figure 2. Characterization of heterogeneous epoxy composites. a) Legend for different ingredients and process parameters considered in the study (colon notation represents base to cross-linker ratio by weight). b) Measured E along the print direction of different ink formulations as function of CF volume fraction with dotted lines corresponding to the results from the micromechanical model. c) Measured α along the print direction of different ink formulations as function of CF volume fraction. d) Measured σ along the print direction of different ink formulations as function of CF volume fraction. e) Measured σ along the print direction for different carbon filler combinations as function of CB volume fraction with a fixed base:cross-linker ratio of 1:0.2 by weight. Data shown here is tabulated in Table S3 (Supporting Information). f) SEM images of different carbon filler combinations (top) and corresponding schematic (bottom) showing the multiscale interactions of the fillers and cross-links. Arrows in SEMs indicate locations of CNTs on the CF surfaces and CBs in the epoxy matrix.

lines in Figure 2b)[43,44] where there is good agreement within the experimental data and the models. Additionally, we tested the effects of different temperatures on E for a subset of composites that represent the different formulations (tr-x/FS and CB/C Composite) (Figure S4, Supporting Information, and SI Methods). The study shows that there is negligible effect on E as we increase the temperature up to ≈160 ^{0}C (Figure S4b,c, Supporting Information).

Figure 2c shows the effect of changing the CF content on the tunable α along the print direction (see Figure S5, Supporting

Information for transverse properties). A tremendous decrease in α is observed as the volume fraction of CFs increase, even reaching low negative values (-19 ± 0.3 ppm °C^{-1}), indicating that the material shrinks as the temperature increases. The average α of the CFs used in this work is -0.5 ppm °C^{-1}.[45] which is ≈40x bigger than the lowest measured α of our composites. Prior work with carbon fillers has shown similar results in which the measured α is orders of magnitudes smaller than the average α of the constituent carbon filler.[46] where this effect is attributed to relative movements between individual fillers due to the internal compression generated by heating. Another factor contributing to the discrepancy of the α values between constituents and composite is the effect of cross-linking densities on the samples. High cross-linking densities of an epoxy matrix restrict the relative movement of the fillers, thus increasing the effective α of the sample, while low cross-linking densities of an epoxy matrix allow for higher relative movement of the fillers, hence reducing the effective α of the sample.[47]

Adding CNTs does not strongly affect E and α (dark outline data in Figure 2b,c), but we observe a significant increase in σ as we add constant CNTs inclusions of 2% v/v (Figure 2d). As an additional means of further tuning σ, we found that reducing the nozzle size (triangle markers ≈200 µm, circle markers ≈410 µm), yields an increase in σ of ≈70% due to the enhanced degree of alignment of the CFs (Figure S2, Supporting Information). Moreover, we observe that the improvement in σ was more noticeable as the ratio between base to cross-linker weight ratio was lower, since the absence of cross-links allows for more conductive pathways to be formed with the carbon fillers.[47] A summary of the resulting E, α, ultimate stress (S^u), and strain to failure (ϵ^u) for longitudinal and transverse print directions is listed in Table S3 (Supporting Information).

2.3. Multiscale Effect for Tuning σ

Based upon the strong dependence of σ on the inclusion of different carbon fillers, we decided to systematically investigate these effects. For this study, we fixed the base to cross-linker ratio to the lowest value (1:0.2) (Figure 2e; Figure S6, Supporting Information), where the dependence was the highest. We included CB as a filler because of its ability to simultaneously tailor rheology.[48,49] and enhance σ.[49–51] First, we consider the effects of the individual carbon fillers where CF formulations on its own are not electrically conductive. However, including only CNTs at a low concentration (2% v/v) results in a significant enhancement (more than five orders of magnitude) of σ. Combining 2% v/v CNTs with 15% v/v CF yields an even further improvement (3-4 orders of magnitude compared to CNTs only) on σ. Replacing the 2% v/v CNT formulations with 4% v/v CB yields a similar improvement on σ. Furthermore, we combined 4% v/v of CB with the 15% v/v CFs formulation and the 2% v/v CNTs + 15% v/v CFs formulation, respectively, and we found an increase of ≈5x on σ compared to either the 2% v/v CNTs + 15% v/v CFs or the 4% v/v CB + 15% v/v CFs formulations. Finally, we evaluate combinations of the maximum allowable concentration (8% v/v) of CB and found that 15% v/v CFs + 8% v/v CB yield a slightly higher σ (≈7x compared to 2% v/v CNTs + 15% v/v CFs or 4% v/v CB + 15% v/v CFs formulations) while not affecting E and α, nor the printability. On the contrary, a 15% v/v CFs + 2% v/v CNTs + 8% v/v CB formulation resulted in a non-printable ink, exhibiting repeated nozzle clogging.

Based on these results, we picture a composite microstructure where the electrical percolation of CF is blocked by the cross-links of the epoxy due to the large size of the CFs relative to the spacing between cross-links (Figure 2fi). Loading the composite with nanoscale carbon fillers, such as CNTs or CB, enables electrical percolation as these fillers are small enough to form networks between cross-links. By adding CFs to these nanocomposites and aligning them by the printing process, we achieve a synergistic effect where the CNTs and CB provide percolation bridges between neighboring aligned CFs (Figure 2fii,iii, respectively), resulting in a large multiscale percolation network, and an order of magnitude increase of σ. Including both nanoscale fillers and CFs can further increase percolation (Figure 2fiv), which further increases σ by around a factor of 2. A similar type of increase of σ can be achieved by adding more of a single nano-filler, as seen in the 8% v/v CB + 15% v/v CFs formulation. This micro-structure concept is further supported by prior related work on carbon composites.[47,52–54] A summary of the resulting σ for longitudinal and transverse print directions is listed in Table S3 (Supporting Information).

2.4. Stiff, Electrically Controllable Self-Sensing Bilayers

To demonstrate the utility of our epoxy composite inks, we used multi-material 4D printing to first create simple bilayers (**Figure 3**), the basic functional unit across all our structures. The curvature responses of these bilayers can be expressed as,[12,55]

$$\delta\kappa\, t_2 = \left(\epsilon_2 - \epsilon_1\right) \frac{6\,\beta\gamma\,(1+\beta)}{1 + 4\beta\gamma + 6\beta^2\gamma + 4\beta^3 + \beta^4\gamma^2} \tag{1}$$

where $\delta\kappa$ is the change in curvature after a temperature change (ΔT), $\beta = t_1/t_2$, $\gamma = E_1/E_2$, $\epsilon_i = \epsilon_{p,i} - \Delta T\alpha_i$, $\epsilon_{p,i}$ is the permanent strain from the curing process for material i (Figure S7, Supporting Information), t_i is thickness of material i, E_i is the elastic modulus of material i, α_i is the reversible CTE for material i, and subscripts 1 and 2 denote low and high CTE materials, respectively. Validation of Equation 1 (Figure S8, Supporting Information) is shown by printing high fidelity bilayers (Figure S9, Supporting Information) with different ink combinations with respect to β and comparing the measured curvature after an imposed temperature change to the prediction. Using Equation 1, we choose a pair of inks to print a bilayer composed of one high α ink that is not electrically conductive (1:1:8 + B), while the other ink possesses negative α and high σ (1:0.2 + 15% v/v CF + 8% v/v CB) allowing us to use this layer as a Joule heating element (Figure 3a). Due to the curing-based permanent shrinkage, the curvature of the transformed state ($T = 25$ °C) of the bilayers is slightly larger than the CTE alone; hence the shrinkage generates a more pronounced curvature response while still maintaining reversibility. When heating the conductive layer via Joule heating, the bilayer structure exhibits a controllable, repeatable, and pronounced actuation response by modulating the Joule heating power (Figure 3b, SI Methods, and Movie M1). We actuate the

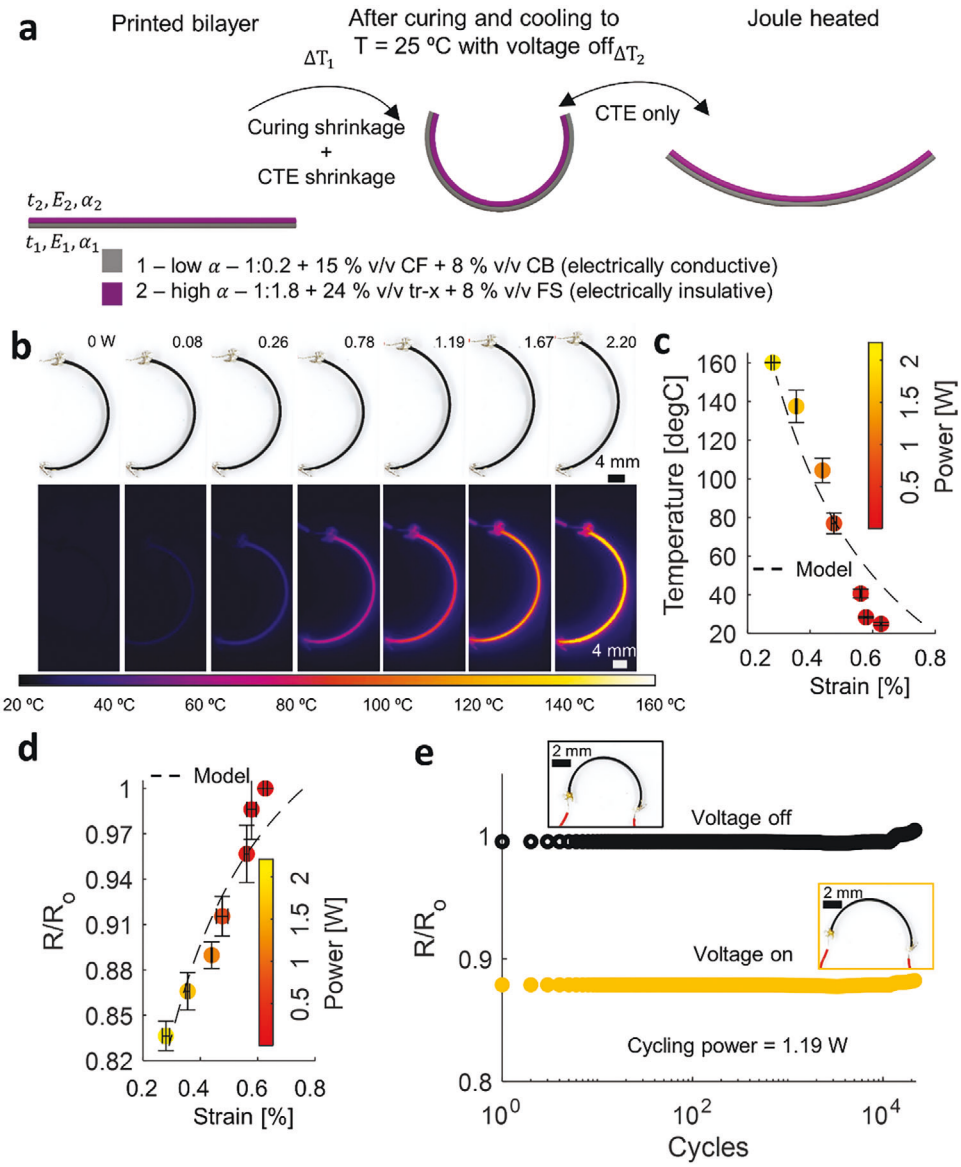

Figure 3. Multimaterial 4D printed electrically controllable bilayers. a) Schematic of electrically controllable bilayer after printing (left), after curing at 250 °C and cooling down to room temperature with ΔT_1 = -225 °C (middle), and after reversibly Joule heating to 160 °C with ΔT_2 = 135 °C (right). b) Optical images of electrically controllable actuation via Joule heating at different power levels (top) with corresponding thermal imaging showing temperature field as function of Joule heating power (bottom). c) Measured (filled circles) and modeled (dotted line) response of temperature and strain with respect to different power levels (error bars represent standard deviation of three tested samples). d) Measured (filled circles) and modeled (dotted line) response of change in electrical resistance ($\Delta R/R_0$) and strain with respect to different power levels (error bars represent standard deviation of three tested samples). e) Measured change in electrical resistance ($\Delta R/R_0$) as function of number of cycles (yellow – voltage on, black – voltage off).

bilayer from room temperature at 0 W, up to 160 °C at 2.2 W. To predict the behavior of these electrically controllable bilayers, we develop an electro/thermal-mechanical model (Supporting Information Methods, Figure 3c,d). The measured surface temperature, curvature, and change in electrical resistance (R/R_o) as a function of the Joule heating power exhibit good agreement with our model (Figure 3c,d). By examining R/R_o, we can observe a one-to-one correlation between the average thermal strain experienced throughout the bilayer (Equation S16, Supporting Information) and the change in the electrical resistance during Joule heating (Figure 3d). Hence, changes in strain and R/R_o can be directly programed with power inputs, allowing us to enable self-sensing capabilities (SI Methods). Further, we characterize the sensitivity of our device (Figure S10, Supporting Information), showing that it achieves a high and repeatable sensitivity with a gauge factor of 40.80 ± 0.82, which is significantly higher than commercially available sensors and comparable to state of the art carbon-based sensors.[56] Figure 3e shows the cycling heating response of our bilayer up to 54% of the maximum tested actuation power. The response is highly repeatable, with more than 20 000 actuation cycles. Unlike other highly sensitive carbon-based sensors.[56] these self-sensing bilayers exhibit no signal

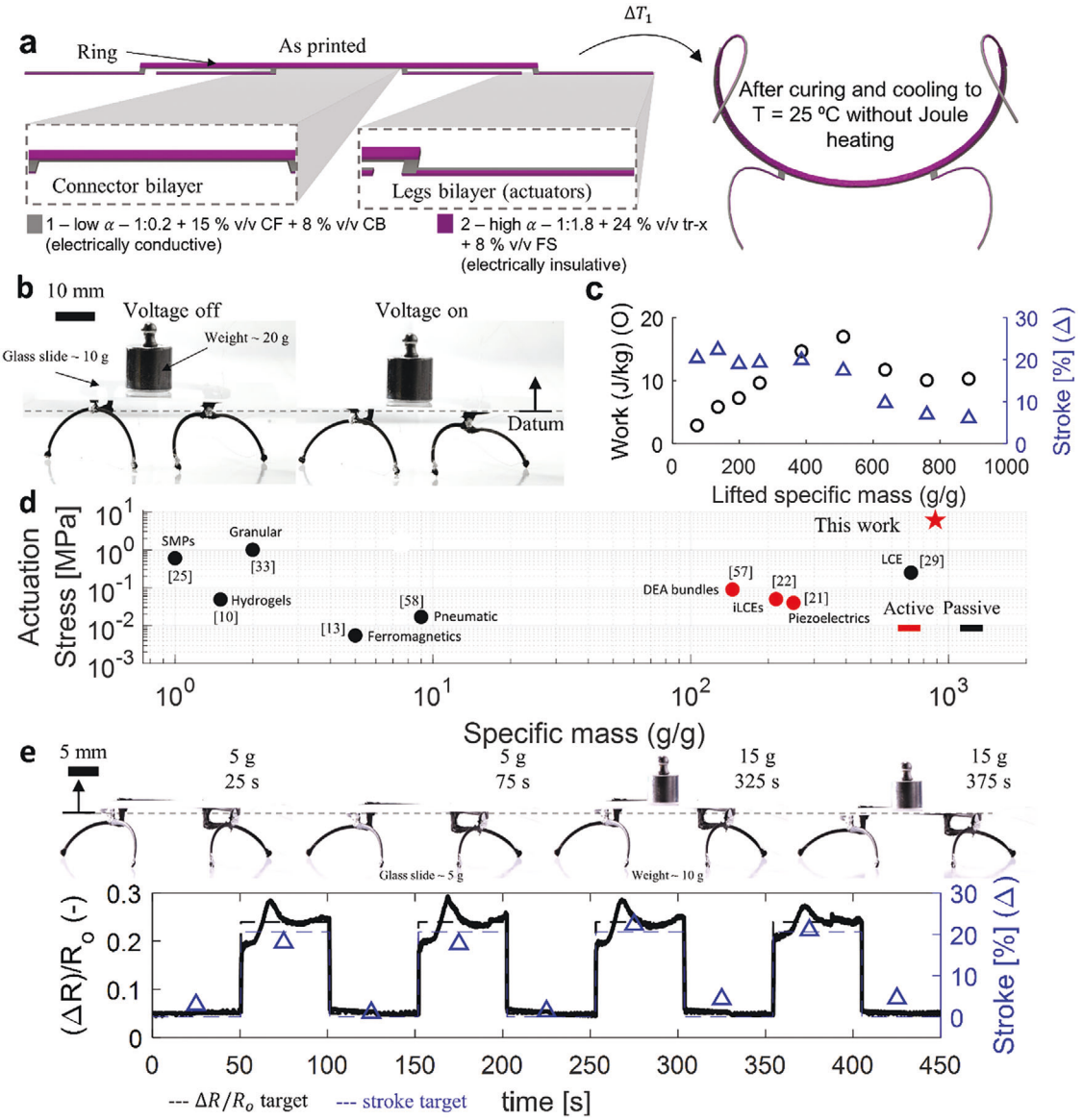

Figure 4. Multimaterial 4D printed weightlifting robot. a) Schematic of the lifting robot after printing (left) and after curing at 250 °C and cooling down to room temperature (ΔT_1 = -225 °C). b) Photographs of lifting robot being actuated, lifting 313 times its own weight. Datum represents the bottom of the stroke and the direction of positive work. c) Measured response of different lifting tests. d) Performance metrics of different 3D printed actuators, where black is passive actuator and red is active actuator. e) Photographs of lifting robot being control via a Proportional-Integral-Derivative (PID) controller, where it was programed to achieve a targeted stroke based on the change in electrical resistance ($\Delta R/R_0$) (top). Measured response (solid lines) of ($\Delta R/R_0$) and stroke (triangles) compared to the programed response (dotted lines) (bottom).

drift due to the immobile carbon filler network, made possible by the stiff epoxy matrix.

2.5. Lifting Robot

To demonstrate the capabilities of these epoxy composites bilayers, we developed a morphable weightlifting robot using 4D multi-material printing (**Figure 4**). We designed a structure that is 3D printed flat (Figure 4a and Movie M2) and deploys to a self-standing table-like configuration after curing when cooled to room temperature (Figure 4a, Movie M3, and Figure S11a, Supporting Information). This design provides the maximum actuation stroke, while maintaining high stiffness (Figure S11b–d, Supporting Information). We used the same two inks as the bilayers in Figure 3 and controlled the structures via Joule heating. The morphing mechanism for the structure consists of multiple bilayers with different functionalities denoted here "connectors" and "actuators", both of which are designed using Equation 1 (SI Methods). The connectors are designed such that when cured and cooled to room temperature, they curl out-plane forming a ring configuration, which was ≈70% of a full circle (Figure S11a, Supporting Information). The actuators were designed to bend in-plane (plane perpendicular to the connectors); thus, these

serve as vertical supports for the structure. The final design is composed of three connectors and four actuators.

Figure 4b illustrates how we evaluated the actuation performance of this robot. The actuation cycle was generated by providing a constant power input (≈2 W) for ≈15 s (≈1 time constant, see SI Methods), followed by a power cut-off and a cooldown interval of ≈25 s (≈2 time constant, see SI Methods). Following, we add external weights (combinations of glass slides and/or calibrated weights) on top of the robot, with gradual increments, to test the performance of the actuation cycle with variable loads (Movie M3). As for performance metrics, we track the specific work, lifted specific mass, and actuation stroke. Figure 4c shows that our lifting robot yield maximum specific work and stroke of 16.99 J kg^{-1} and 22.29%, respectively, while lifting a maximum weight of 885.90 times its own weight. This current design can maintain its targeted 20% stroke up to 470 times its own weight. After this point, the reversible stroke is reduced by additional deflections on the actuator legs due to the heavy loads. Unlike prior work, all these tests were performed on a self-standing configuration, thus, the actuation nature of this structure generated pushing forces rather than pulling forces, which is difficult to achieve with soft materials.

Figure 4d shows the actuation stress and specific mass for relevant prior work on 3D-printed responsive actuators.[10,13,21,22,25,29,33,57,58] The various actuators are differentiated based on how the stimulus for actuation is generated: via change in environment conditions through additional components (passive) (e.g., hot plates, ovens, external magnets, water bath) or using internal stimuli (active) (e.g., voltage). Comparing our robot with the highest performance passive 3D printable actuator, ours shows improvements of 24x and 1.24x on actuation stress and specific mass, respectively. Similarly, comparing our robot with the highest performance active 3D printable actuator, ours shows improvements of 150x and 3.55x on actuation stress and specific mass, respectively. Notably our results stand out significantly with the highest actuation stress and specific mass capacity amongst the active actuators, due to the intrinsic electrical properties of our materials (Figure 4d; Tables S4 and S5, Supporting Information). Finally, comparing the performance of our robotic actuators to commercially available ones, ours is the fifth-highest performing actuator (in both actuation stress and specific lifted mass) out of nineteen different types (Figure S12, Supporting Information).

Given that these actuators are highly responsive and possess self-sensing capabilities (Figure 3), we explored regulating their actuation response via closed-loop control (Figure 4e and Movie M4). Specifically, a PID control system is programed with a target $\Delta R/R_o$ that autoregulates the lifting robot to reach different targets through time (Figure S11e, Supporting Information), even with large external weight disturbances (Figure 4e). We designated a target square wave trajectory with $\Delta R/R_o$ of 5% and 23%, corresponding to target strokes of ≈3% and ≈20%, respectively, and periods of 50 s, which is ≈4.2 times bigger that the time constant for this system (SI Methods). The system rapidly adjusts the power to achieve the target output, such that the $\Delta R/R_o$ responses lie within 4.79% and 0.77% overshoot and undershoot, respectively. Notably, this robot can achieve targeted actuation while experiencing disturbances more than 170 times its own weight.

2.6. Stiff Shape-Shifting Lattices

To use our material palette for morphing planar structures into complex target shapes, we arrange multiplexed pairs of bilayers into a heterogenous lattice in which we have control of the initial distance between nodes ($\tilde{L}$) and the number of cells (N) within the lattice of the printed structures, and the initial sweep angle ($\tilde{\theta}_i$) of every rib, which is considered an independent degree of freedom and is indexed throughout the lattice to achieve targeted designs (Figure S13, Supporting Information)[12] The linear growth factor (s) for these structures can be expressed as,[12]

$$s_i = \frac{L}{\tilde{L}} = \frac{2sin\left(\frac{1}{4}\,\tilde{\theta}_i\,\left(2+\frac{\tilde{L}\delta\kappa}{sin\left(\tilde{\theta}_i/2\right)}\right)\right)}{2sin\left(\tilde{\theta}_i/2\right)\,+\,\tilde{L}\delta\kappa} \tag{2}$$

where L is the new distance between nodes due to $\delta\kappa$ (from Equation 1). Up to four different materials are used in the cross-section, which allows us to program the intrinsic and extrinsic curvatures of the resulting shapes[12] We demonstrate the efficacy of this approach for our new material system by printing flat square lattices that morph into self-standing spherical caps (Figures S14–S16, Supporting Information), saddles, and alternating gaussian and mean curvatures (Figure S17, Supporting Information). A comprehensive characterization of different targeted spherical caps is reported in Table S6 (Supporting Information). Unlike prior work using soft 4D printed materials, these materials do not sag under their own weight. We achieve large self-standing spherical caps of ≈200 mm width and ≈200 mm length, which is 11 times larger in projected area than prior work (Figure S16, Supporting Information). Based on preliminary calculations of scaling analysis, we envision that our structures can be printed as large as ≈1000 mm x 1000 mm without reaching sagging, which would be ≈3 orders of magnitude larger than prior work with soft 4D printed materials (SI Methods).

To show the capability of our approach to create shapes with complex geometrical features and self-standing structures, we printed a planar lattice that transform into a self-supported human face (**Figure 5a**; Figure S18, Supporting Information). Similar to prior work, we choose to replicate C.F. Gauss face.[12] starting with a 3D target surface mesh generated from a painting of Gauss through a machine learning algorithm.[59] We conformally projected the face to the plane and discretized the planar projection using a lattice with $\tilde{L}$ = 10 mm and with the number of cells in the width (N_x) and length (N_y) of 17 and 26, respectively (Movie M5). The lattice discretization and associated inverse-design procedure follows the approach detailed in.[12] but using material properties from our new heterogeneous polymer composites. We find among all ribs the maximum and minimum required growth factors to be s = 1.46 and s = 0.44, respectively. The largest growth factors are required near the nose and the chin, where the target mesh has the most substantial Gaussian curvature. To evaluate the accuracy of our printed face, we generated a 3D reconstruction of the transformed face using laser-scanning techniques. By fitting the scan data with our target mesh, we can compute the smallest distance from each point on the scanned face to the target shape. Using this as an error metric, we normalize it as the error/$\tilde{L}$. The distribution of the error/$\tilde{L}$ exhibits a 95% confidence interval within ± 0.519, which is ≈16% more accurate

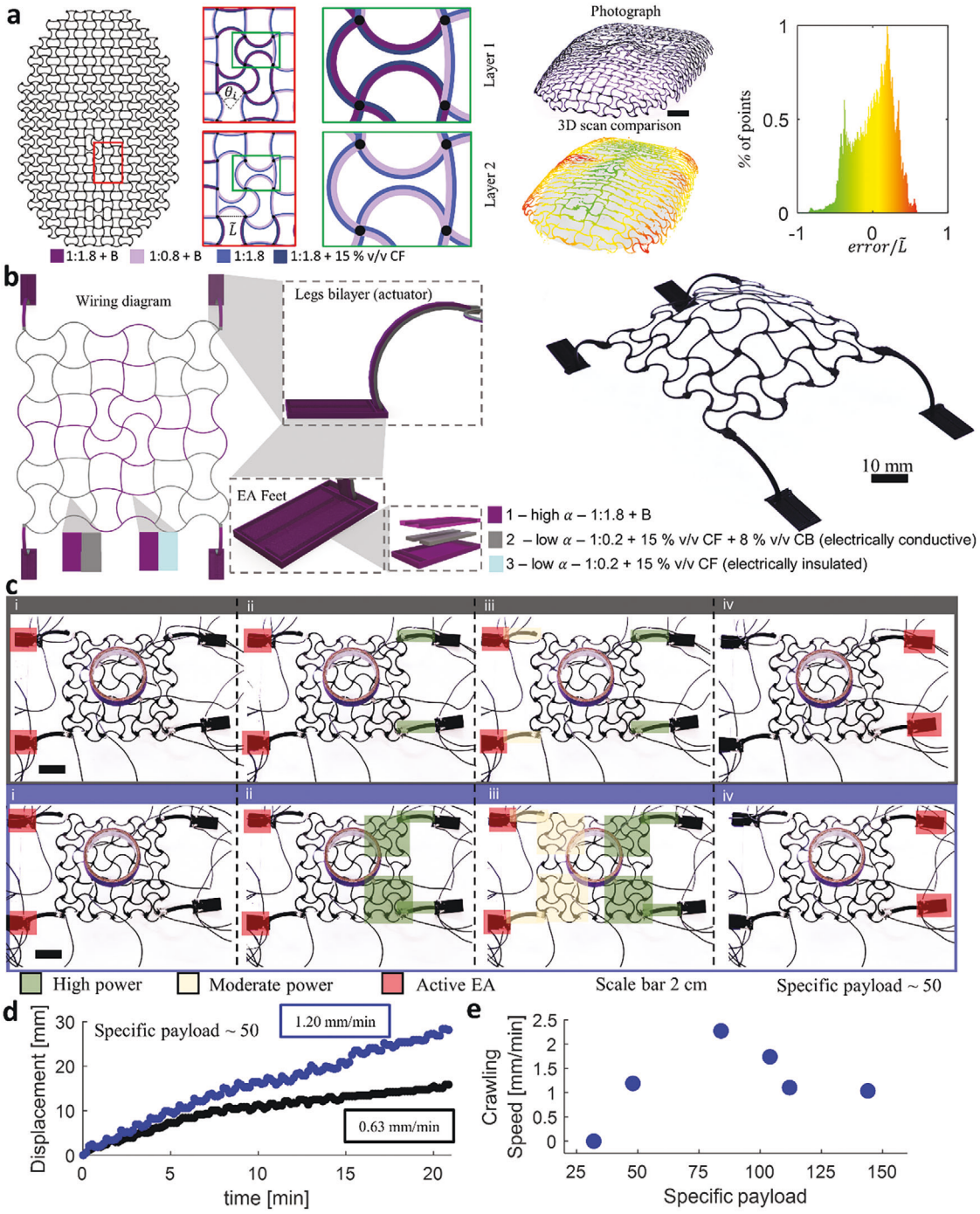

Figure 5. Integrated design and fabrication of a multifunctional 3D lattice structures. a) Inverse design highlights for 4D printing a flat lattice to shift into the 3D likeness of Carl Friedrich Gauss (left). Photograph of lattice after transformation (Scale bar is 20 mm in length) (middle-top). 3D scan of the printed face superimposed onto target shape with colors representing the normalize error (error/$\tilde{L}$) between the 4D printed shape and the target shape (middle – bottom). Shades of green indicate regions where the 4D printed lattice lies below the target shape while red indicates regions where it lies above the target. (right) Distribution of error/$\tilde{L}$. b) Schematic of 4D printed robotic lattice with crawling capabilities (left). The body consists of a lattice body structure, where the legs are bilayers, and the feet are electro adhesive (EA) pads. Isometric view photograph of 4D printed crawling robot (right). c) Top view photographs of different crawling modes showing the actuation sequences. The first mode consists of only the legs been used to advance the robot forward (top) and the second mode is the combination of the legs and body (bottom) (scale bars are 2 cm). (i) The actuation sequence for both gait modes starts by activating the posterior EA feet to anchor the device to the substrate. (ii) Then the anterior actuator legs are actuated at maximum power (2.64 W) for ≈10 s. (iii) While maintaining the anterior actuator legs engaged, we activated the posterior actuators at 75% of the maximum power and wait for ≈10 s. (iv) Then we simultaneously disengage the posterior EA feet, engage the anterior EA feet, and cut off power of anterior and posterior actuators and wait for ≈30 s until it cools to room temperature, dragging its own body forward toward the anterior EA feet. d) Measured displacement from crawling tests as a function of time. E) Measured speeds for the body and legs actuation mode with different specific payloads.

than prior work[12] Notably, we showed that we can maintain the high accuracy of the 4D printing method while enhancing the mechanical behavior of the transformed structures to enable big, stiff, and complex self-standing shape-shifting structures.

2.7. Electrically Controlled Robotic Lattices

To further test the multifunctionality of our approach, we combine the electrically responsive actuators (Figures 3 and 4) and 4D printed lattices (Figure 5a; Figures S14–S16, Supporting Information) to develop an electrically controlled robotic lattice capable of multiple modes of crawling locomotion (Figures 5b; Figure S19, Supporting Information). We chose three different materials, one non-conductive with high α (1:1.8 + 24% v/v tr-x + 8% v/v FS), and two with much lower values of α, one of which is electrically conductive (1:0.2 + 15% v/v CFs + 8% v/v CB) and the other is electrically insulative (1:0.2 + 15% v/v CFs). Using these materials, we print a planar square lattice that deploys to a spherical cap, containing conductive pathways within the lattice to electrically activate sections of the structure (Movie M6). The structure is a flat square lattice with $\tilde{L} = 15$ mm and $N = 6$, with $\tilde{\theta}_i$, programed via stereographic projection.[12] to transform into a spherical cap with an opening angle of 135^0. This larger opening angle was selected to maximize Gaussian curvature, which provides an enhanced mechanical advantage by achieving higher stiffness compared to planar structures.[60,61] The lattices possess four electrically isolated conductive quadrants, which allow individual control of each section of the morphing surface. To improve the actuation stroke, we add simple bilayers to each corner of the lattice, referred to here as "legs". These legs function to lift and support the lattice body and can be individually actuated. Finally, we print four Electro Adhesive (EA) pads denoted here as "feet", to enhance the adhesion between the substrate and the locomotive lattice (Movie M7).[62,63]

Figure 5c shows two different gaits modes that we tested on this robot. The first gait mode (Figure 5c top panel and Movie M8) consisted of using only the bilayer legs of the robot as the actuators, while the second gait mode (Figure 5c bottom panel and Movie M9) uses the combined stroke generated by the bilayer legs and the lattice body. The actuation sequence for both gait modes (Figure 5c) starts by activating the posterior EA feet to anchor the device to the substrate (Figure 5ci). Then, the anterior actuator legs are actuated at maximum power (2.64 W) for ≈10 s (Figure 5cii). While maintaining the anterior feet and legs engaged, we activated the posterior legs at 75% of the maximum power and waited for ≈10 s (Figure 5ciii); this ensures that the forces generated by the actuator legs are lower than the adhesive forces of the EA feet.[62] Then, we simultaneously disengage the posterior EA feet, engage the anterior EA feet, cut off the power of anterior and posterior actuators (Figure 5civ), and wait for ≈30 s (≈2 time constant, see SI Methods) until all parts of the robot cool to room temperature, dragging its own body forward toward the anchored anterior EA feet. Figure 5d shows the displacement of the robotic lattice over time for the two types of gaits at a fixed specific payload (weight of payload over the weight of robot) of ≈50. The resulting crawling speed of the combined mode (body + legs) is 1.90 times faster than the single actuation mode (legs only). This improvement is attributed to the combined displacement generated by the bilayer legs and the lattice body. Furthermore, we evaluated the payload capacity with respect to crawling speed for the faster gait strategy (legs + body) (Figure 5e). We found that carrying an external load up to 84 times its own weight onto the lattice optimally enhances the crawling speed (Figure 5e), which can be attributed to an increase in the adhesion force between the substrate and the robot due to a higher normal force.[62] thus reducing the slipping between the robot and the substrate. After a specific load of 84, the speed gets reduced by ≈50%. This reduction can be attributed to carry loads that are higher than the actuation stress capacity of the actuators (legs + body) (Movie S9, Supporting Information), hence hindering the locomotion speed. Nonetheless, increasing the specific load further demonstrates that the robot still achieves forward locomotion up to a payload of 144 times its own weight.

3. Limitations and Future Work

While this work has presented tremendous contributions for the development of new stiff, electrically controllable materials suitable for DIW, several avenues for future research emerge from this study to expand the utility of these materials. First, the demonstrations in this work are currently limited to print flat thin sheets that deploy into pre-programed 3D shapes. Printing responsive volumes would allow us to achieve a higher level of resulting complexity for a broader range of applications. This could be achieved by employing new printing processes, such as embedded 3D printing.[30] to our materials palette to achieve volumetric 4D printing via DIW. Second, our current stiff and responsive materials are brittle (i.e., possess failure strains less than ≈1%) and exhibit relatively low toughness (K) (≈0.01 to 1 MJ m^{-3}) compared to existing 3D printed actuators (ranging from ≈ 0.05 to ≈9 MJ m^{-3}; see Table S4, Supporting Information). We envision future work to investigate strategies that improve these properties for our materials, while preserving their high stiffness. This endeavor would realize a new class of 4D printed materials that are stiff, tough, and damage-tolerant.

4. Conclusion

We have developed new heterogeneous polymer composites for 4D printing with high stiffness, tunable coefficient of thermal expansion (α), and electrical conductivity (σ). We demonstrate that printed bilayers of these materials exhibit programable and predictable thermal and mechanical responses, with high gauge factor self-sensing while being actuated via Joule heating. These materials enable the fabrication of a new type of stiff lifting actuators with highly repeatable self-sensing capabilities, which allows the implementation of closed-loop control for modulated actuation, with specific load capacities up to 885.90 times its own weight. This robot shows improvements of 150x and 3.55x on actuation stress and specific mass, respectively, compared to existing 3D printed active actuators. Furthermore, comparing the performance of our robotic actuator to 3D printed commercially available actuators, ours is the fifth highest performance actuator out of nineteen different types. We show that these materials can be combined with multi-material 4D printing of lattice structures to develop large, stiff, and complex shape-shifting structures. Combining the multifunctionalities of these materials with

the morphing lattice approach, we develop a stiff, electrically controllable shape-shifting robotic lattice with multiple crawling locomotion modes. With further development, these materials can be implemented into new composite structural designs to develop stronger, autonomous morphing systems such as sensors, actuators, antennas, and robots.

5. Experimental Section

Materials: All non-CNTs inks were created by mixing (DAC 150.1 FVX-K, FlackTek, 60 s at 3500 rpm) appropriate amounts of base and cross-linker of epoxy (SUP121 AO, Master Bond), prior mixing additional ingredients. Using these mixtures, isotropic inks were obtained by only adding fumed silica (Aerosil 150, Evonik), ranging from 6 – 9% v/v and mixing (DAC 150.1 FVX-K, FlackTek) for 180 s at 3500 RPMs with cooling down steps of 60 s, every 60 s. Surfactant (Triton x-100, Sigma Aldrich) inks were created by mixing the different surfactant concentrations (20% v/v and 24% v/v) at 3500 RPM for 30 s (DAC 150.1 FVX-K, FlackTek), following by the addition of fumed silica (Aerosil R 106, Evonik), ranging from 6 – 9% v/v and mixing (DAC 150.1 FVX-K, FlackTek) for 90 s at 3500 RPMs with cooling down steps of 30 s, every 30 s. Inks containing CF (K223HM, Mitsubishi Chemical, diameter ≈11 µm, length ≈200 µm) were created by mixing (DAC 150.1 FVX-K, FlackTek for 60 s at 3500 RPMs) fumed silica (Aerosil 150, Evonik) ranging from 6 – 9% v/v, following by the addition of the appropriate amount of CF (5 – 15% v/v) with the epoxy mixtures, and mixing (DAC 150.1 FVX-K, FlackTek) for 180 s at 3500 RPMs with cooling down steps of 60 s, every 60 s. For the CNTs inks, a premixture of CNTs (NH2 functionalized multi-walled CNTs, Cheap Tubes, diameter ≈20 nm, length ≈10 µm) with epoxy base was first made by adding ≈1 – 2% v/v of CNTs to the base epoxy and ball milling (High energy ball mill Emax, Retsch) for 8 h at 3200 RPMs, with a mass ratio of 3 to 1 between mixing balls (stainless steel grinding balls, diameter ≈2 mm, Retsch) and premixture, respectively. Mixed materials and mixing balls were separated after mixing using a customized filtering procedure. The procedure consisted of inserting stainless steel metal round filters (9317T136, McMaster) placed at the bottom of a 20-cc syringe (7510A45, McMaster), followed by adding the mixture of the base epoxy/CNTs and stainless-steel mixing balls and extruding the material through the filter onto a 40 cc mixing cup (DAC 150.1 FVX-K, FlackTek). All premixtures were stored in a freezer at – 40 °C. Inks containing CNTs inclusions were created by adding the appropriated amounts of the premixture base with CNTs and cross-linker, followed by the mixing (DAC 150.1 FVX-K, FlackTek) of the appropriate amount of CFs for 180 s at 3500 RPMs with cooling down steps of 60 s, every 60 s. Last, inks containing CB (Carbon black, acetylene, 100% compressed, 99.9%, Thermo Scientific Chemicals) were created by adding the proper amount of corresponding base (no CNTs or CNTs) to cross-linker, following with the addition of corresponding CFs, and mixing (DAC 150.1 FVX-K, FlackTek) for 180 s at 3500 RPMs with cooling down steps of 60 s, every 60 s. The pot life of all these epoxy composite inks is about three days, thus, there is no concern that the rheology changes while making the inks. All the inks were loaded into Luer-Lock syringes (3cc or 10cc, Nordson, EFD), then centrifuged (300 s at 4000 RPMs) to remove air bubbles before printing. A summary of ink formulations is listed in Table S2 (Supporting Information).

Multimaterial 4D Printing: Inks were mounted in Luer-Lock syringes (Norson, EFD), as stated in the material section. Each syringe was mounted to one of the four independently controlled z-axes of a multi-axis motion system (Aerotech Inc.), equipped with tapered nozzles ranging from 200 – 410 µm inner diameter (Nordson, EFD). A custom solenoid (VQD1151-5MO- M5, SMC Pneumatics) array was connected to a pressure controller (Ultimus V, Nordson EFD), which serves to turn the pressure to the syringes on or off. Solenoids were individually connected to the syringes, allowing motion-synchronized individual on/off control for the extrusion of each ink throughout the printing process. Custom, open-source Python libraries (Mecode).[64] were used to define each ink's print path and coordinate printhead motion with ink extrusion. All samples were printed onto Teflon-coated steel substrates. Extrusion printing pressures (HPx High-Pressure Dispensing Tool, Nordson EFD) and speeds ranged from 210 – 490 psi and 15 – 25 mm s^{-1}, respectively. After printing, all samples were cured in an oven (HeraTherm, Thermo Scientific) at 250 °C for 120 min. The oven was preheated for ≈1.5 h to achieve uniform heating of the entire oven volume at 250 °C. This preheating method allows for the fastest heating rate, primarily facilitated by the transfer of heat from the oven's interior to the samples. As a result, this strategy ensures that the heating rate significantly outpaces the curing rate.

Thermal Expansion, Electrical, and Elastic Modulus Measurements: Samples (8 mm long, 2 mm wide, and 2 mm tall) were printed to characterize the CTE for each of the inks (Figure S5, Supporting Information), following the standardized testing method ASTM E228 – 17.[65] Each sample was tested in a push-rod dilatometer (DiL, C-THERM) from room temperature, up to 250 °C, with a heating rate of 10 °C min^{-1}. The CTE was determined by fitting the data with the linear relationship $\epsilon_{thermal} = \alpha \Delta T$ via MATLAB's *"polyfit"* function. The resulting thermal strain versus change in temperature data is presented in Figure S5 (Supporting Information). A summary of the resulting longitudinal CTE for each sample is given in Figure 2c, with the error bars representing the 95% confidence interval of the fits. A summary of the results for longitudinal and transverse CTE is reported in Table S3 (Supporting Information). Samples (8 mm long, 2 mm wide, and 2 mm tall) were printed to characterize σ for each of the conductive inks. Thin wires (38 awg) were glued with commercially available silver epoxy (MG Chemicals 8331D) to the ends of each sample. Then a four-point method was utilized to measure the electrical resistance across the width and length of each sample. Three samples were tested per ink composition. The electrical conductivity of each sample was determined using the following relation $\sigma = A/LR$, where A is the cross-sectional area of each sample, L is the length of each sample, and R is the electrical resistance of each sample. A summary of the resulting σ along the longitudinal for each sample is given in Figure 2d, with the error bars representing the standard deviation on the measurement. A summary of the σ along longitudinal and transverse is presented in Table S3 (Supporting Information). Tensile test samples (gauge length ≈9.50 mm, wide ≈3.20 mm, and thickness ≈1.60 mm) were printed to characterize the elastic modulus of each ink, following standardized methods ASTM D0638 – 14.[66] Each sample was tested under uniaxial tension in a single-axis mechanical tester (Instron 5944 Micro-tester) at an engineering strain rate of 1.38×10^{-4} s^{-1} for engineering strains from 0 to 0.02 (Figure S3, Supporting Information). The resulting engineering stress versus strain data is represented in Figure S3c (Supporting Information). The elastic modulus (E) for each sample was determined by fitting low strain data ($0 \leq \epsilon \leq 0.005$)[67] to the linear relationship $\sigma = E\epsilon$ via the "*polyfit*" function in MATLAB. A summary of the resulting longitudinal E for each sample is given in Figure 2b, with error bars representing the standard deviation of the measurements. Three samples were tested per ink formulation. A summary of the strain to failure (ϵ^u), ultimate stress (S^u), and young modulus (E) for longitudinal and transverse samples are reported in Table S3 (Supporting Information).

SEM Imaging: CTE samples were cryofractured to generate small fragments for imaging. The imaging on the fracture points was focused, allowing a clear image of the cross-section of the samples. Imaging was performed using a Field Emission Scanning Electron Microscope (FESEM) (Supra 40 VP, Zeiss). An Electron High Tension (EHT) voltage of 4k-5k volts was used to get a clear contrast of the carbon fillers on the epoxy matrix.[41,68] with a working distance ranging from 10.60 to 12.00 mm and an aperture size of 30 µm.

Electrothermomechanical Characterization of Bilayers: Simple bilayers constructs of low α – 1:0.2 + 15% v/v CF + 8% v/v CB (print speed = 20 mm $^{-1}$s, extrusion pressure = 210 psi, nozzle size = 200 µm) and high α – 1:1.8 + 24% v/v tr-x + 8% v/v FS (print speed = 15 mm $^{-1}$s, extrusion pressure = 175 psi, nozzle size = 200 µm) were printed to test electrothermomechanical responses and lifespan. These samples each had printed width, length, and total thickness of ≈2 mm, ≈40 mm, and ≈0.8 mm, respectively. After printing, samples were cured in an oven (HeraTherm, Thermo Scientific) for 120 min at 250 ^{0}C. Following this, thin copper wires (awg 38) were glued with commercially available silver epoxy (MG Chemicals 8331D), enabling a reliable interface with the testing electronics.

Following this, it was proceeded to test the electrothermomechanical response of these via Joule heating. The bilayers were electrically connected to a power supply (E36233a, Keysight), where the voltage was limited at 30 V and the current was modulated from 5 – 105 mA with increments of 14.3 mA, allowing 60 s on each step to reach a steady state temperature. For the electrical response, the change in electrical resistance was tracked by reading the current passing through and the voltage drop across the bilayer. Optical imaging was performed with a calibrated camera (D850, Nikon), to obtain side images of the curvature response of the bilayers due to Joule heating. The curvature of each sample was extracted from each frame using Hough transform "imfindcircles" on MATLAB, which fits a circle with 95% of confidence of interval to the side view of a bilayer. Thermal imaging was carried out using an IR camera (A600-Series, FLIR), and their temperature was extracted (ResearchIR, FLIR) using an emissivity of 0.95[69] The thermal images in Figure 3b correspond to the steady state point of actuation (≈60 s after actuation started). Cycling data was performed following a procedure similar to the curvature characterization, only adjusting the power from 0 to 1.19 W (corresponding to 0–70 mA). Joule heating was active for 30 s (≈3 time constant, see SI Methods) at 1.19 W and then cut off power for 60 s (≈5 time constant, see SI Methods) to allow cooldown to room temperature. A similar optical image procedure was used to obtain side images, where a custom Python script was developed to retrieve 20 images per decade.

Electrothermomechanical Modeling of Bilayers: The model consisted of three physical elements: convective cooling, electro-thermal behavior, and thermo-mechanical response. For the convective cooling element, the assumption of lumped system was started with due to the small dimensions of the samples (Biot number ≈0.01), which allows to assume a uniform temperature distribution across the body. Heat generation is given from the core of the conductive filament due to Joule heating. Heat losses were assumed to be by natural convection and Nusselt correlations for vertical and horizontal plates were used accordingly.[69] For the electro-mechanical element, the change in electrical resistance was described by combining geometry and temperature change.[22] For the thermo-mechanical behavior, the internal stress and strain generated by the change in temperature were considered. The expression developed by Timoshenko for bi-metal thermostats was used and slightly adapted to the system (SI Methods).[12,55] Finally, the different elements were coupled into a custom MATLAB script to calculate the combined response due to the different phenomena (SI Methods). The results of the modeling are shown in Figure 3c,d.

Lifting Robot Design: The lifting robot consisted of several bilayers designed to deploy into a stable ring configuration (Figure 4). It was started by designing the bilayers acting as the actuator legs to achieve the maximum actuation stroke while maintaining high structural stiffness. Two different designs were considered for the bilayers that were used for the legs. First, the legs were modeled as shape-shifting arcs where the stroke was given by the change in chord length due to the change in the opening angle. For the second consideration, the legs were modeled as a cantilever beam in which the stroke was given by the change in tip deflection given by internal stress due to a temperature change. For both, the possibility of orienting the legs with an angle (θ) with respect to the vertical axis (Figure S11b, Supporting Information), was considered. The mechanical response for the legs was modeled as the axial stiffness of a beam (K) (SI Methods). Figure S11c,d (Supporting Information) shows a summary of the design results (SI Methods). The change in leg length (L) was studied within lower and upper bounds of 10 mm and 35 mm, respectively. A dimensionless variable for the designing angles was used, where the ratio was given by the rotation angle with respect to the vertical axis (θ) and the opening angle (θ_p) of the bilayer (θ/θ_p). Following this, the bilayers used for the ring body ("connectors"), which provides structural stability to the device, were designed. With Equation 1, the curvature response for the deployed state ($T = 25$ °C) was calculated. These results were used to determine the opening angle for a given length of the bilayer, and then the results for the legs designs were combined and it was calculated that there was a need of three connectors to reach ≈70% of a circle configuration in the deployed state, allowing to reach a structural stable resting state due to the resulting axisymmetric structure. The lifting robot was printed using a low α – 1:0.2 + 15% v/v CF + 8% v/v CB (print speed = 20 $mm^{-1}s$, extrusion pressure = 105 psi, nozzle size = 410 µm) and high α – 1:1.8 + 24% v/v tr-x + 8% v/v FS (print speed = 15 $mm^{-1}s$, extrusion pressure = 84 psi, nozzle size = 410 µm). The connectors length, width, and total thickness were ≈35 mm, ≈1.5 mm, and ≈1.7 mm, respectively. The legs length, total width, and thickness were ≈30 mm, ≈0.9 mm, and ≈0.9, respectively.

Lifting Robot Characterization: The legs were electrically insulated by using a nonconductive ink (1:1.8 + 24% v/v tr-x + 8% v/v FS) as the interface between the legs and the connectors. Pairs of thin copper wires (awg 38) were glued with commercially available silver epoxy (MG Chemicals 8331D) to each leg, creating an electrical interface with the power supply and the device. To characterize the electrothermomechanical response, the legs were connected to a power supply (E36233a, Keysight), where the voltage was limited to 30 Volts and the electrical current was modulated from 0 to 380 mA. A calibrated optical camera (D850, Nikon) was used for imaging the front view of the test sample, to determine the vertical displacement of the structures. The vertical displacement was extracted from the images (MATLAB) and normalized by the cord length of the legs to determine the vertical stroke. Structures were activated at maximum stroke (≈2 W) for ≈15 s (≈1 time constant, see SI Methods), followed by a cut off from power to cool down to room temperature for 60 s (≈5 time constant, see SI Methods). A glass slide was placed on top of the robot structure, to provide a platform to load the robot with external weight. Increments of external weight ranging from 5–70 g (glass slides and calibrated weights), were added onto the device, to test the stroke performance over various external payloads. External weights were normalized by the actuator mass (≈80 mg total mass of 4 legs). A summary of the results from the characterization is shown in Figure 4c.

Lifting Robot Closed Loop Control: Proportional, integral, derivative (PID) closed loop control was implemented using a custom Python script, to program electrical current and measure the voltage drop across the lifting robot (E36233a, Keysight) (Figure S11e, Supporting Information). Electrical current was limited from 10 to 380 mA to maintain a heat generation lower than T = 250 °C, to avoid thermal degradation. The target $\Delta R/R_o$ was input in the control script, and the target L/L_o was estimated given the target $\Delta R/R_o$ and the electro-thermal actuation characterization (Figure 3). The sampling rate of the loop was set to be 1000 Hz, which was four orders of magnitude faster than the thermal response of the lifting robot (SI Methods). PID gains were determined using the system identification toolbox (MATLAB). The PID gains (K_p, K_d, and K_i) were found to be 0.008, 0.0005, and 0.0002, respectively. Images used to measure response stroke were captured (Nikon D850) every 1 s and analyzed using a custom image analysis script in MATLAB. External weights were normalized by the actuator mass (≈80 mg total mass of four legs).

Face Reconstruction and Error Analysis: To generate a 3D reconstruction of the experimentally transformed face, the lattice was placed onto the print bed of the custom printer. Then a laser scanner (LJ-X8000A, Keyence) was attached to an automated gantry (Aerotech Inc.). Through a customized set of commands, the lattice was scanned, and the position data of the gantry was synchronized with the laser scanner, resulting in the 3D reconstruction of the transformed face. Following this step, the scanned data was imported into an open-source point cloud processing software (CloudCompare). Here the point cloud was processed and denoised by performing a density computation and discarding isolated points. Then the target shape mesh in the same software was imported, scaled it to its pre-computed physical size given the lattice dimensions and the global scaling factor, and aligned the bounding boxes of the point cloud with the scaled target mesh. To perform the distance computation, a finer alignment of the point cloud was performed with the target mesh according to the Iterative Closest Point (ICP) algorithm (translation and rotation only). Then the closest distance for each point in the point cloud of the scanned face to the target mesh according to the built-in routine of CloudCompare was computed and exported the histogram data of this quantity was exported.

Locomotive Lattice Design: Samples were prepared using one high α ink (1:1.8 + 24% v/v tr-x + 8% v/v FS) (print speed = 15 $mm^{-1}s$, extrusion pressure = 175 psi, nozzle size = 200 µm) and two low α inks where one was electrically insulated (1:0.2 + 15% v/v CF)

(print speed = 25 $mm^{-1}s$, extrusion pressure = 210 psi, nozzle size = 200 µm) and the other is electrically conductive (1:0.2 + 15% v/v CF + 8% v/v CB) (print speed = 20 $mm^{-1}s$, extrusion pressure = 210 psi, nozzle size = 200 µm), while both have similar α and E (≈-3 ppm $°C^{-1}$ and ≈33 GPa, respectively) to maintain thermal responsiveness. The body was designed as a square flat lattice that deploys into a self-standing semi-spherical cap with $\tilde{L}$ = 15 mm, N = 6, and opening angle of 135^0 (SI Methods). Electrically conductive pathways were designed within the lattices to achieve individual control of the four different sections of the body. Bilayers (printed width, length, and total thickness of ≈1.6 mm, ≈40 mm, and ≈ 0.8 mm, respectively) that act as legs on each corner were designed similar to the bilayers used as an actuator in Figures 3 and 4. EA pads (printed width, length, and total thickness of ≈10 mm, ≈35 mm, and ≈0. m, respectively) were printed separately using an electrically insulated ink (1:1.8 + 24% v/v tr-x + 8% v/v FS) and an electrically conductive ink (1:0.2 + 15% v/v CF + 8% v/v CB). The devices were cured in an oven (HeraTherm, Thermo Scientific) for 120 min at 250 °C. Copper wires (30 awg) were glued to the electrodes of the EA pads using commercially available silver epoxy. Similarly, copper wires (30 awg) were glued to the legs and body of each section of the robot. Following, we cast the same epoxy formulation (1:0.2 base to cross-linker by weight with no fillers) was cast to electrically insulate the EA pads from the legs and, at the same time, glued the tip of the bilayer legs to the EA pads. The assembly of the EA pads and body was cured in an oven (HeraTherm, Thermo Scientific) overnight at 150 °C.

The different sections of the locomotive lattice were controlled using an array of four NPN power transistors (TIP102, STmicroelectronics), as shown in Figure S19 (Supporting Information). The transistors were all connected in parallel, with each transistor connected in series with a section of the locomotive lattice and a power source (E36233a, Keysight), and to a common ground. The sections were divided into combinations of bilayer leg + body and bilayer leg only, where the ground was alternated between the end of the body section or the end of the leg, respectively (Figure S19, Supporting Information). To actuate the target section of the lattice, a 5 V signal was applied to the base connection of the transistor using an Arduino Uno. The voltage supply was 17 V with a current of 600 mA. The switch shown in Figure S18 (Supporting Information) represents the manual switching of the sections of the locomotive lattice being actuated, with one modality of actuation being only the legs, and another one being the body and the legs together. An array of 4 high voltage DC to DC converters (Q60 – 5, XP Power) were used for controlling the actuation of the EA feet. The gain of the DC-to-DC converter was 1.2k from input voltage to output voltage. The input voltage was 2.99 volts, which translates to 3.59 kilovolts, just below the electric breakdown field of the epoxy.[37]

Locomotive Lattice Characterization: A calibrated camera (D850, Nikon) was positioned to track a top view of the crawling motion. The stage was a metal plate with a white coating to allow for higher contrast between the background and the test samples. Electronics were placed on a custom breadboard next to the stage, with sufficiently long wire length to not affect the robot's motion. An Arduino One was programed with two gait modes, which execute actuation when turned on. A calibrated ruler was positioned inside the frame of the camera to track the displacement. Displacement and time data were extracted from the images using a custom script (MATLAB). Hollow cylinder tapes were used as weights. These were loaded onto the body, taking advantage of the dome-like structure to keep from falling while crawling. External weights were normalized by the actuator mass (≈250 mg total mass of actuators (legs + body)).

Supporting Information

Supporting Information is available from the Wiley Online Library or from the author.

Acknowledgements

The authors gratefully acknowledge support from the National Science Foundation CAREER Award (CMMI-2047683; J.W.B) and the AFOSR Young Investigator Award (FA9550-20-1-0365; J.W.B., R.E.S.C.), National Defense Science and Engineering Graduate (NDSEG) fellowship program (J.M.M.F). This work used the shared experimental facility BioInterface Technologies (BIT) Facility. The authors thank the Fluid Lab, especially Professor J. Bird and G. Lee, for technical assistance on thermal imaging. The authors also thank S.F. Zopf and X. Ye for their helpful discussion and technical assistance.

Keywords

4D printing, actuators, autonomous structures, metamaterials, morphing structures, robotic lattices

Received: April 17, 2024
Published online: May 20, 2024

[1] S. M. Mirvakili, I. W. Hunter, *Adv. Mater.* **2018**, *30*, 1704407.
[2] S. H. Kim, M. D. Lima, M. E. Kozlov, C. S. Haines, G. M. Spinks, S. Aziz, C. Choi, H. J. Sim, X. Wang, H. Lu, D. Qian, J. D. W. Madden, R. H. Baughman, S. J. Kim, *Energy Environ. Sci.* **2015**, *8*, 3336.
[3] S.-H. Song, J.-Y. Lee, H. Rodrigue, I.-S. Choi, Y. J. Kang, S.-H. Ahn, *Sci. Rep.* **2016**, *6*, 21118.
[4] S. M. Mirvakili, I. W. Hunter, *Adv. Mater.* **2017**, *29*, 1604734.
[5] M.-S. Kim, J.-K. Heo, H. Rodrigue, H.-T. Lee, S. Pané, M.-W. Han, S.-H. Ahn, *Adv. Mater.* **2023**, *35*, 2208517.
[6] D. Kim, I. Ferretto, C. Leinenbach, W. Lee, *Adv. Mater. Interfaces* **2022**, *9*, 2200171.
[7] A. N. Alagha, S. Hussain, W. Zaki, *Mater. Des.* **2021**, *204*, 109654.
[8] J. M. Jani, M. Leary, A. Subic, M. A. Gibson, *Mater. Des. 1980–2015* **2014**, *56*, 1078.
[9] S. Tibbits, *Archit. Des.* **2014**, *84*, 116.
[10] A. Sydney Gladman, E. A. Matsumoto, R. G. Nuzzo, L. Mahadevan, J. A. Lewis, *Nat. Mater.* **2016**, *15*, 413.
[11] X. Kuang, D. J. Roach, J. Wu, C. M. Hamel, Z. Ding, T. Wang, M. L. Dunn, H. J. Qi, *Adv. Funct. Mater.* **2019**, *29*, 1805290.
[12] J. W Boley, W. M. van Rees, C. Lissandrello, M. N. Horenstein, R. L. Truby, A. Kotikian, J. A. Lewis, L. Mahadevan, *Proc. Natl. Acad. Sci. U. S. A.* **2019**, *116*, 20856.
[13] Y. Kim, H. Yuk, R. Zhao, S. A. Chester, X. Zhao, *Nature* **2018**, *558*, 274.
[14] B. G. Compton, J. A. Lewis, *Adv. Mater.* **2014**, *26*, 5930.
[15] A. Kotikian, R. L. Truby, J. W. Boley, T. J. White, J. A. Lewis, *Adv. Mater.* **2018**, *30*, 1706164.
[16] T. van Manen, S. Janbaz, A. A. Zadpoor, *Mater. Horiz.* **2017**, *4*, 1064.
[17] K. Saito, S. Nomura, S. Yamamoto, R. Niiyama, Y. Okabe, *Proc. Natl. Acad. Sci. U. S. A.* **2017**, *114*, 5624.
[18] D. S. Adams, M. Mobrem, *J. Spacecr. Rockets* **2009**, *46*, 403.
[19] T. G. Bifano, J. Perreault, R. Krishnamoorthy Mali, M. N. Horenstein, *IEEE J. Sel. Top. Quantum Electron.* **1999**, *5*, 83.
[20] M. Piovarči, et al., In Proc. of the 1st Annual ACM Symp. on Computational Fabrication, **2017**, 1.
[21] H. Cui, D. Yao, R. Hensleigh, H. Lu, A. Calderon, Z. Xu, S. Davaria, Z. Wang, P. Mercier, P. Tarazaga, X. R. Zheng, *Science* **2022**, *376*, 1287.
[22] A. Kotikian, J. M. Morales, A. Lu, J. Mueller, Z. S. Davidson, J. W Boley, J. A. Lewis, *Adv. Mater.* **2021**, *33*, 2101814.
[23] M. Rashed Khan, G. J. Hayes, J.-H. So, G. Lazzi, M. D. Dickey, *Appl. Phys. Lett.* **2011**, *99*, 013501.
[24] S. Weng, X. Kuang, Q. Zhang, C. M. Hamel, D. J. Roach, N. Hu, H. Jerry Qi, *ACS Appl. Mater. Interfaces* **2021**, *13*, 12797.
[25] Q. Ge, A. H. Sakhaei, H. Lee, C. K. Dunn, N. X. Fang, M. L. Dunn, *Sci. Rep.* **2016**, *6*, 1.
[26] D. J. Roach, X. Sun, X. Peng, F. Demoly, K. Zhou, H. J. Qi, *Adv. Funct. Mater.* **2022**, *32*, 2203236.

[27] C. Liu, H. Qin, P. T. Mather, *J. Mater. Chem.* **2007**, *17*, 1543.
[28] C. P. Ambulo, J. J. Burroughs, J. M. Boothby, H. Kim, M. R Shankar, T. H. Ware, *ACS Appl. Mater. Interfaces* **2017**, *9*, 37332.
[29] S. Li, H. Bai, Z. Liu, X. Zhang, C. Huang, L. W. Wiesner, M. Silberstein, R. F. Shepherd, *Sci. Adv.* **2021**, *7*, eabg3677.
[30] X. Peng, S. Wu, X. Sun, L. Yue, S. M Montgomery, F. Demoly, K. Zhou, R. R. Zhao, H. J Qi, *Adv. Mater.* **2022**, *34*, 2204890.
[31] Y. Zhang, Q. Wang, S. Yi, Z. Lin, C. Wang, Z. Chen, L. Jiang, *ACS Appl. Mater. Interfaces* **2021**, *13*, 4174.
[32] Y. Jiang, L. M. Korpas, J. R. Raney, *Nat. Commun.* **2019**, *10*, 128.
[33] S. Eristoff, S. Y. Kim, L. Sanchez-Botero, T. Buckner, O. D. Yirmibesoglu, R. Kramer-Bottiglio, *Adv. Mater.* **2022**, *34*, 2109617.
[34] H. Cui, D. Yao, R. Hensleigh, H. Lu, A. Calderon, Z. Xu, S. Davaria, Z. Wang, P. Mercier, P. Tarazaga, X. R. Zheng, *Science* **2022**, *376*, 1287.
[35] M. Li, A. Pal, A. Aghakhani, A. Pena-Francesch, M. Sitti, *Nat. Rev. Mater.* **2022**, *7*, 235.
[36] Y. Wang, Z. Wang, Q. He, P. Iyer, S. Cai, *Adv. Intell. Syst.* **2020**, *2*, 1900177.
[37] Master Bond Inc. Supreme 121AO Technical Data Sheet.
[38] R. E. Jensen, E. O'Brien, J. Wang, J. Bryant, T. C. Ward, L. T. James, D. A. Lewis, *J. Polym. Sci. Part B: Polym. Phys.* **1998**, *36*, 2781.
[39] S. R. Swan, H. Gan, C. Creighton, J. M. Griffin, B. V. Gashi, R. J. Varley, *J. Appl. Polym. Sci.* **2022**, *139*, e52854.
[40] R. P. White, J. E. G. Lipson, *Macromolecules* **2016**, *49*, 3987.
[41] H. A. Pierson, E. Celik, A. Abbott, H. De Jarnette, L. Sierra Gutierrez, K. Johnson, H. Koerner, J. W. Baur, *Exp. Mech.* **2019**, *59*, 843.
[42] R. Kulkarni, O. Ochoa, *J. Compos. Mater.* **2006**, *40*, 733.
[43] B. Raju, S. R. Hiremath, D. Roy Mahapatra, *Compos. Struct.* **2018**, *204*, 607.
[44] H. Ghazisaeidi, xx xx, **2006**.
[45] xx xx, **2021**.
[46] K. Shirasu, G. Yamamoto, I. Tamaki, T. Ogasawara, Y. Shimamura, Y. Inoue, T. Hashida, *Carbon* **2015**, *95*, 904.
[47] J. H. Choi, H. J Song, J. Jung, J. W. Yu, N.-H. You, M. Goh, *J. Appl. Polym. Sci.* **2016**, *134*, 44253.
[48] K. Lakdawala, R. Salovey, *Polym. Eng. Sci.* **1987**, *27*, 1035.
[49] D. Ren, S. Zheng, F. Wu, W. Yang, Z. Liu, M. Yang, *J. Appl. Polym. Sci.* **2014**, *131*, 39953.
[50] A. Chortos, E. Hajiesmaili, J. Morales, D. R. Clarke, J. A. Lewis, *Adv. Funct. Mater.* **2020**, *30*, 1907375.
[51] J. T. Muth, D. M. Vogt, R. L. Truby, Y. Meng, D. B. Kolesky, R. J. Wood, J. A. Lewis, *Adv. Mater.* **2014**, *26*, 6307.
[52] H. Lu, W. Min Huang, *Appl. Phys. Lett.* **2013**, *102*, 231910.
[53] M. Wen, X. Sun, L. Su, J. Shen, J. Li, S. Guo, *Polymer* **2012**, *53*, 1602.
[54] K. Ke, L. Yue, H. Shao, M.-B. Yang, W. Yang, I. Manas-Zloczower, *Carbon* **2021**, *173*, 1020.
[55] S. Timoshenko, *J. Opt. Soc. Am.* **1925**, *11*, 233.
[56] C. S. Boland, U. Khan, G. Ryan, S. Barwich, R. Charifou, A. Harvey, C. Backes, Z. Li, M. S. Ferreira, M. E. Möbius, R. J. Young, J. N. Coleman, *Science* **2016**, *354*, 1257.
[57] A. Chortos, J. Mao, J. Mueller, E. Hajiesmaili, J. A. Lewis, D. R. Clarke, *Adv. Funct. Mater.* **2021**, *31*, 2010643.
[58] M. Schaffner, J. A. Faber, L. Pianegonda, P. A. Rühs, F. Coulter, A. R. Studart, *Nat. Commun.* **2018**, *9*, 878.
[59] A. S. Jackson, et al., In Proc. of the IEEE Int. Conf. on computer vision, **2017**, 1031.
[60] J. Chilton, G. Tang, *Routledge* **2016**.
[61] P. Grönquist, P. Panchadcharam, D. Wood, A. Menges, M. Rüggeberg, F. K. Wittel, *R. Soc. Open Sci.* **2020**, *7*, 192210.
[62] G. Gu, et al., *Sci Robot* **2018**.
[63] J. Shintake, S. Rosset, B. Schubert, D. Floreano, H. Shea, *Adv. Mater.* **2016**, *28*, 231.
[64] J. Minardi, Available at, https://github.com/jminardi/mecode/.
[65] E37 Committee. ASTM International.
[66] D20 Committee. ASTM International.
[67] R. C. Hibbeler, *Mechanics of Materials* **2017**, Pearson.
[68] J. R. Raney, B. G. Compton, J. Mueller, T. J. Ober, K. Shea, J. A. Lewis, *Proc. Natl. Acad. Sci.* **2018**, *115*, 1198.
[69] T. L. Bergman, F. P. Incropera, *Fundamentals of heat and mass transfer 7e: heat transfer*, Wiley Custom Learning Solutions, Hoboken, NJ **2011**.